Additional Information	NOTICE: This is the author's version of a work that was accepted for publication in Surface and Coatings Technology. Changes resulting from the publishing process, such as peer review, editing, corrections, structural formatting, and other quality control mechanisms may not be reflected in this document. Changes may have been made to this work since it was submitted for publication. A definitive version was subsequently published in Surface and Coatings Technology, Vol. 206, (21). 15th June, 2012. http://dx.doi.org/10.1016/j.surfcoat.2012.02.060
Alternative Location	http://dx.doi.org/10.1016/j.surfcoat.2012.02.060

Accepted Manuscript

Evaluation of microhardness, fracture toughness and residual stress in a thermal barrier coating system: A modified Vickers indentation technique

W.G. Mao, J. Wan, C.Y. Dai, J. Ding, Y. Zhang, Y.C. Zhou, C. Lu

Please cite this article as: W.G. Mao, J. Wan, C.Y. Dai, J. Ding, Y. Zhang, Y.C. Zhou, C. Lu, Evaluation of microhardness, fracture toughness and residual stress in a thermal barrier coating system: A modified Vickers indentation technique, *Surface & Coatings Technology* (2012), doi: 10.1016/j.surfcoat.2012.02.060

Evaluation of microhardness, fracture toughness and residual stress in a thermal barrier coating system: A modified Vickers indentation technique

W. G. Mao [a,b,c]*, J. Wan [a,c], C. Y. Dai [a,c]*, J. Ding [a,c], Y. Zhang [a,c], Y. C. Zhou [a,c], C. Lu [d]

[a] Key Laboratory of Low Dimensional Materials & Application Technology, Ministry of Education, Xiangtan University, Hunan 411105, China

[b] Aeronautical Science and Technology Key Laboratory of Aeronautical Test and Evaluation, Nanchang Hangkong University, Jiangxi 330063, China

[c] Faculty of Materials, Optoelectronics and Physics, Xiangtan University, Hunan 411105, China

[d] Department of Mechanical Engineering, Curtin University, Western Australia 6845, Australia

* Corresponding authors: W. G. Mao, E-mail: ssamao@126.com. C. Y. Dai, E-mail: daicuiying@xtu.edu.cn

Abstract

The evolution of microhardness, fracture toughness and residual stress of an air plasma-sprayed thermal barrier coating system under thermal cycles was investigated by a modified Vickers indentation instrument coupled with three kinds of indentation models. The results show that fracture toughness on the top coating surface after thermal cycles changes from 0.64 to 3.67 MPa·m$^{1/2}$, and the corresponding residual stress near the indented region varies from –36.8 to –243 MPa. For the interface region of coating and bond coat, fracture toughness in the coating close to interface ranges from 0.11 to 0.81 MPa·m$^{1/2}$, and residual stress varies from –5 to –30 MPa, which are consistent with available data. For the lateral region of coating, fracture toughness and residual stress display strong gradient characteristics along the thickness direction due to the special layered structure.

Highlights

We proposed a modified Vickers indentation instrument by re-designing load intervals.
Microhardness, fracture toughness and residual stress of coating were measured.
Mechanical properties display strong gradient characteristics along thickness direction.
The method has a large advantage to study the failure of coating/film materials.

Keywords

thermal barrier coating; fracture toughness; residual stress; Vickers indentation, microhardness

1. Introduction

Thermal barrier coatings (TBCs) have attracted an ever-increasing attention in aircraft and industrial gas-turbine applications owing to their excellent wear resistance, corrosion protection and thermal insulation. They can prolong the operation life of metal substrate and enhance thermal efficiency of engines [1,2]. Many studies have shown that the evolution of interface adhesion, thermal/residual stresses and mechanical properties of TBCs are crucial to predict their durability and reliability in service [1,3-5]. Thus, three intrinsic parameters of a TBC system, including hardness, fracture toughness and residual stress, are urgent to be tested by using a simplified and low-cost method. Recently, a lot of methods such as barb pullout, bending, scratch, X-ray diffraction, Raman spectroscopy and indentation tests have been developed. Compared to these tests, the indentation method can measure microhardness, residual stress and fracture toughness of bulk brittle materials [6-10], which is also used to test a few of brittle film/ductile substrate systems [11-14]. However, in the case of a multiple-layer TBC system, if residual stress and fracture toughness are expected to be synchronously studied by indentation fracture models proposed by Lawn *et al.* [15], traditional indentation instruments may not be directly applied due to the lack of enough suitable indentation loads. As the best of our knowledge, there is still no reported work in which residual stress and fracture toughness of a TBC system can be simultaneously tested by a Vickers indentation method.

In this paper, we attempt to modify a Vickers indentation instrument by re-designing the value and interval of loads, and then use it to study the evolution of microhardness, residual stresses and fracture toughness of an air plasma-sprayed (APS) TBC system subjected to thermal cycling, including the top surface, lateral and interface regions of the coating. Further, the effects of thermal cycling, coating thickness and indentation locations on mechanical properties of a TBC system have been discussed. The experimental results are in agreement with available data.

3

2. Theoretical models

2.1. Indentation model

As indentation load increases, a brittle material gradually experiences elastic and little plastic deformation, and then fracture. Once the stress intensity factor K_I in an indented material approaches its fracture toughness K_{IC}, a pair of radial cracks usually start to nucleate near the corner angles of residual Vickers indentation and finally present a semiellipse shape along the indentation direction [6,7,10], as shown in Fig. 1. Here, K_{IC} can be evaluated, in the case of no residual stress [6], as

$$K_{IC} = \delta \left(\frac{E}{H} \right)^{1/2} \frac{P}{c^{3/2}} \quad (c \gg d) \tag{1}$$

where δ is a geometric factor and for a Vickers indenter, $\delta = 0.016$ [6], $c = (c_1 + c_2)/2$ is the average length of two radial cracks with lengths of c_1 and c_2 (see Fig. 1(a)). E and H are Young's modulus and hardness of the indented material, respectively. In Vickers indentation tests, hardness is usually calculated by $1.8544 P / d^2$, where P is the peak indentation load and d is equal to $(d_1 + d_2)/2$ with d_1 and d_2 defined as the two diagonal lengths of residual Vickers indentation, as shown in Fig. 1(a).

Residual stresses with gradient distribution characteristic usually exit in the indented region for a coating/film system due to the mismatch of material properties and temperature variation, which may strongly affect the accuracy of indentation measurements. For the sake of simplification, the distribution of residual stresses is divided into small strips along the indentation direction and they are approximately regarded as uniform in each small strip. The effect of total residual stress on stress intensity factor can be evaluated in the indentation depth by an integral method. An analytical solution proposed by Lawn *et al*. is applied to describe the influence of residual stress in a strip on stress intensity factor, which can be written as [16],

$$K_r = \psi \sigma_r c^{1/2} \left[2 \left(b / c + t / c \right)^{1/2} - 2 \left(b / c \right)^{1/2} - t / c \right] \tag{2}$$

where σ_r is the distributed uniform average tensile residual stress at a small strip along the

indentation depth direction, $\psi = 2/\sqrt{\pi}$ is a crack geometry term [17], b is the distance from the strip to the indented surface, and t is the depth of the distribution region of σ_r. When the stress layer locates on surface (i.e., $b = 0$), Eq. (2) reduces to

$$K_r = \psi \sigma_r \sqrt{t}(2 - \sqrt{t/c}) \qquad (3)$$

If the strip extends to the thorough indentation crack region (i.e., $b = 0$, $d = t$), Eq. (3) reduces to

$$K_r = \psi \sigma_r c^{1/2} \qquad (4)$$

which is similar to the result for a uniform stress field. According to the different distribution features of residual stresses in the indented material, we should select a suitable equation from Eq. (3) or (4) to analyze the effect of residual stress on K_r.

For residual stress in a TBC system, it is generally simplified as in-plane equi-biaxial stress and out-plane gradient stress along the thickness direction [18]. Therefore, in the case of indentation perpendicular to the coating surface (see Fig. 1(a)), residual stress is assumed to be uniformly distributed in a narrow strip just below the indented surface. The corresponding stress intensity factor K_r induced by residual stress at the crack front can be estimated by Eq. (3). Therefore, the total stress intensity factor are the superimposition of K_r and K_p, which can be written as [16]

$$K_{IC} = K_r + K_p = \chi \frac{P}{c^{3/2}} + \frac{4}{\sqrt{\pi}} \sigma_r t^{1/2} - \frac{2}{\sqrt{\pi}} \sigma_r t / c^{1/2} \qquad (5)$$

where $\chi = \delta (E/H)^{1/2}$. Then, the ratio $P/c^{3/2}$ can be obtained as

$$\frac{P}{c^{3/2}} = \left(\frac{K_{IC} - \dfrac{4}{\sqrt{\pi}} \sigma_r t^{1/2}}{\chi} \right) + \left(\frac{2t\sigma_r}{\chi\sqrt{\pi}} \right) c^{-1/2} \qquad (6)$$

which is regarded as a function of $c^{-1/2}$. Here, $2t\sigma_r / \chi\sqrt{\pi}$ and $(K_{IC} - 4\sigma_r t^{1/2} / \sqrt{\pi}) / \chi$ denotes the slope and intercept of Eq. (6), respectively. To obtain a better linear equation, a series of Vickers

indentation tests must be performed under different peak indent loads. The corresponding radial crack lengths are measured by the Vickers instrument with the function of an in-situ microscope observation system, i.e., $P_i / c_i^{3/2}$ versus $c_i^{-1/2}$ ($i = 1, 2, ..., n$). Then, all experimental data are fitted into a linear equation. K_{IC} and σ_r at the indented point can be determined by the magnitude of intercept and slope of the equation, respectively. It is found that the indentation fracture of APS 8.0 wt% Y_2O_3-partially-stabilized ZrO_2 (8YSZ) coating on the surface regions usually occurs under the load of 78.4 N or more. Otherwise, indentation cracking does not occur because load is too small. On the other hand, if the indentation load is too large, the ceramic coating would be directly broken down and spalled. Therefore, in the case of a TBC system, in order to perform a reasonable range of indentation loads with a small interval, we have re-designed a commercial indentation instrument and adjusted its range and interval of indentation loads.

2.2. Interfacial indentation model

As shown in Fig. 1(b), when a Vickers indenter is penetrated into the interface of two different materials, fracture toughness for the coating/bond coat interface is usually evaluated as [19]

$$K_{IC} = \delta \left(\frac{E}{H} \right)_i^{1/2} \frac{P}{c^{3/2}} \tag{7}$$

where δ is a geometric factor and δ = 0.015 for a Vickers indenter, and $(E/H)_i^{1/2}$ is a ratio of reduced Young's modulus and hardness of two indented materials. If the occupied areas of the coating and bond coat in residual impression are equal, $(E/H)_i^{1/2}$ is defined as [19]

$$\left(\frac{E}{H} \right)_i^{1/2} = \frac{(E/H)_c^{1/2}}{1+(H_c/H_s)^{1/2}} + \frac{(E/H)_s^{1/2}}{1+(H_s/H_c)^{1/2}} \tag{8}$$

where subscripts s and c are bond coat and coating, respectively. However, when the occupied area ratio is not equal in indentation tests, Eq. (8) is hard to describe the effects of two different materials on

indentation resistance. Therefore, it is necessary to consider the indenter trace near the interface with a ratio of lengths z_1 and z_2 (see Fig. 1(b)). The diagonal lengths of residual indentation for coating and bond coat are defined as

$$d_c = \frac{z_1}{z_1 + z_2} d_1 \quad \text{and} \quad d_b = \frac{z_2}{z_1 + z_2} d_1 \tag{9}$$

where d_1 is defined as the total length of an indent diagonal whose direction is vertical to the indented interface. Considering the influence of plastic deformation [20,21], $(E/H)_i^{1/2}$ can be approximately written as [21]

$$\left(\frac{E}{H}\right)_i^{1/2} = \frac{z_1}{(z_1 + z_2)}(E/H)_c^{1/2} + \frac{z_2}{(z_1 + z_2)}(E/H)_s^{1/2} \tag{10}$$

On the other hand, according to the in-plane equi-biaxial stress assumption, the distribution of residual stresses for lateral indentation (see Figs. 1(b) and (c)) can be regarded as uniform along the indentation orientation. In this case, K_r induced by residual stress can be approximately evaluated by Eq. (4). Therefore, the total fracture toughness for lateral indentation can be expressed as a sum of K_p and K_r [22], that is

$$K_{IC} = K_p + K_r = \delta \left(\frac{E}{H}\right)_i^{1/2} \frac{P}{c^{3/2}} + \frac{2}{\sqrt{\pi}} \sigma_r c^{1/2} \tag{11}$$

Similar to Eq. (6), we have

$$\frac{P}{c^{3/2}} = \left(\frac{K_{IC}}{\chi_i}\right) + \left(-\frac{2\sigma_r}{\sqrt{\pi}\chi_i}\right) c^{1/2} \tag{12}$$

where $\chi_i = \delta (E/H)_i^{1/2}$, and $P/c^{3/2}$ is regarded as a linear function of $c^{1/2}$. $-2\sigma_r / \sqrt{\pi}\chi_i$ and K_{IC}/χ_i denotes the slope and intercept of this linear equation, respectively. Here, σ_r is tensile if the slope is negative, and otherwise, σ_r is compressive. It is worth noting that, when $z_2 = 0$ in Eq. (9), it means that the Vickers indenter only indents the cross-sectional region of the coating, as shown in

7

Fig. 1(c). In this case, χ_i in Eq. (12) is equal to $\delta(E/H)_c^{1/2}$. Similarly, all experimental data, $P_i / c_i^{3/2}$ versus $c_i^{1/2}$ ($i = 1, 2, ..., n$), can be obtained by Vickers indentation tests under different loads. Then, these data are fitted into a linear equation. Similarity, K_{IC} and σ_r within the lateral or interfacial region of the coating can be estimated by the values of intercept and slope, respectively.

3. Experimental

3.1. *Specimen*

In our experiments of TBCs, substrate is nickel-base super alloy (GH3030) and its dimension is 20 $\times$ 5 $\times$ 2.4 mm^3. A NiCrAlY powder with grain size of 20–50 μm was sprayed to the substrate surface as bond coat with the thickness of about 150 μm by using the low pressure plasma-sprayed technique. The top coating was deposited by the air plasma-sprayed technique with 8YSZ powder that has the same grain size of 20–50 μm, and the coating thickness is in a range of 400–600 μm. The substrate temperature was held at 473 K during the preparation process [23].

To simulate the effect of high temperature environment on material properties and microstructure of TBCs, most of TBC specimens were performed by heat treatments. They were heated about 10 min up to a desired temperature of 1273 K and then held for 60 min, followed for a 10 min of forced-air-quenching. After polished with 2.5 μm diamond sandpapers, the specimens were cleaned by hydrochloric acid and distilled water to reduce the influence of surface work hardening. All specimens were carefully cleaned by ultrasonic oscillator and completely dried by a drying machine, prior to the microstructure observations, nanoindentation and Vickers indentation tests. The total 120 specimens were tested by using the modified Vickers indentation device.

3.2. *Young's modulus*

The variations of Young's modulus *E* of TBC samples under thermal cycling were measured by

the aid of nanoindentation with an indenter (Triboscope, Hysitron Inc.) equipped with a three-sided pyramidal diamond tip. The tip radius is about 200 nm and the peak load is 3 N. The loading and unloading times are 100 s and the holding time is 20 s. To obtain reliable data, each cycle is repeated 20 times. The thermal drift is kept below ± 0.05 nm/s for all indentations. For 8YSZ coating with many pores and microcracks, the Weibull analysis was introduced to describe the scatter of mechanical properties [24-26]. The detailed analysis has been reported in our recent works [27,28].

3.3.   Vickers indentation

We have re-designed the peak loads and intervals of a commercial Vickers indentation instrument (HVS-30). A series of indentation loads ranged from 9.8 to 294 N with a fitted interval of 19.6 N were selected to induce the formation of different radial cracks at room temperature. In each Vickers indentation test, the dwelling time is 20 s and unloading time is 15 s. All images of residual impressions were observed and the lengths of Vickers indentation cracks were measured by the apparatus with *in-situ* microscopy and charge coupled device camera.

4.   Results and discussion

4.1.   Young's modulus and microhardness

As shown in Fig. 2, Young's modulus E on the top coating surface gradually increases from about 50 GPa (as-received specimens) to 90 GPa within 150 thermal cycles, and then decreases to 59 GPa after 300 thermal cycles. In the lateral region of the coating, E exhibits a similar change and is slightly larger than that on the coating surface. It varies from the initial value of 67 to 120 GPa within 150 thermal cycles. As thermal cycle adds up to 300, the value of Young's modulus is 79 GPa. The major reason for the evolution of Young's modulus of the coating may attribute to the gradient variation of sintering-induced micro-porosity under heat treatments, which displays the anisotropic characteristic of the coating with laminated structures. Young's modulus in the bond coat also changes with thermal

9

cycling. It increases from 79 GPa at the as-received stage to 149 GPa at the 100th thermal cycle, and then retains as a constant. The initially rapid change may be due to high-temperature oxidation. Zhu *et al.* found that the effective Young's modulus of TBCs varies within a range of 60 to 125 GPa under different heat treatments [29,30]. The values of Young's modulus of bond coat in our tests were similar to the results obtained by Haynes [31].

As seen in Fig. 3, the evolution of micro-hardness *H* in the coating by Vickers indentations has a similar trend. *H* on the coating surface increases from 2.76 to 5.84 GPa within about 180 thermal cycles, and then reaches 4.4 GPa. In the lateral region, *H* changes from 3.87 to 6.14 GPa when thermal cycling is within about 150. *H* gradually deceases to 4.71 GPa during subsequent cycles, which are also in consistent with available data [29,32]. Moreover, it is shown that the variation of hardness in the bond coat increases from the as-received 3 to 4 GPa with the increase of thermal cycles due to the interface oxidation under high temperatures, which are well consistent with available data [31].

4.2. *Effect of thermal cycling*

Heat treatments have an important influence on material properties and stress fields of a TBC system during thermal cycles. When indented on the coating surface (see Fig. 1(a)), data of $P_i / c_i^{3/2}$ versus $c_i^{-1/2}$ were fitted with the form of Eq. (6) under different thermal cycles (see Fig. 4). It is obvious that the slope of each fitted line is negative. As the thermal cycle *N* increases from 0 to 180, their corresponding slopes gradually increase from -0.26×10^6 to -1.47×10^6 N/m and intercepts change from 35.56×10^6 to 196.45×10^6 N/m$^{3/2}$. However, after 180 thermal cycles, the slope reduces to the initial state. A representative scanning electron microscopy (SEM) observation of residual impression morphology is shown in Fig. 5, in which there are several radial cracks along the indent diagonal direction and a few of pores.

In interfacial Vickers indentation tests (see Fig. 1(b)), all data were fitted by a linear function of

$P_i / c_i^{3/2}$ and $c_i^{1/2}$ in Eq. (12), as shown in Fig. 6. Within 150 thermal cycles, the slope of each line increases from 79×10^6 to 403×10^6 N/m^2, and then becomes 138×10^6 N/m^2 at N = 300. The corresponding intercept varies from 2.62×10^6 to 10×10^6 N/m$^{3/2}$ and decreases to 1.36×10^6 N/m$^{3/2}$ at N = 300. Fig. 7 shows a typical SEM image of residual Vickers indentation at the coating and bond coat interface. The residual impression is enlarged separately, as shown in inset of Fig. 7, and there are two radial indentation cracks in the coating close to interface.

To study the gradient behavior of material properties along thickness, the lateral region of coating is only indented (see Fig. 1(c)), where L is defined as a distance from the centre of residual impression to the upper surface of coating. Fig. 8 shows the variations of slope and intercept of each fitted line. The analysis indicates that the slope of each line changes within a range of 309×10^6 to 2006×10^6 N/m^2, and the corresponding intercept varies from 4.70×10^6 to 21.0×10^6 N/m$^{3/2}$ during thermal cycles. The SEM morphology of residual impression is shown in Fig. 9, where two radial Vickers indentation cracks and many pores are observed.

4.3. Fracture toughness and residual stress

As discussed above, K_{IC} and σ_r at different indented locations of TBC samples can be evaluated with the values of slope and intercept of each fitted line by Eq. (6) or (12). When indented on the coating surface (see Fig. 1(a)), K_{IC} gradually increases from the initial value of 0.64 to 3.67 MPa·m$^{1/2}$ before 180 thermal cycles, as shown in Fig. 10, which is consistent with the results of 1.15 ± 0.07 MPa·m$^{1/2}$ obtained by asymmetric four-point bending tests [33,34]. After 180 thermal cycles, K_{IC} slowly decreases to 0.91 MPa·m$^{1/2}$. It is of interest to see that the relationship of K_{IC} and thermal cycle presents the parabola evolution and the fitted equation is $K_{IC} = 0.82 + 0.04N - 1.34\times10^{-4}N^2$. The corresponding σ_r in Fig. 11 changes from the deposition stress of –36.8 MPa to a maximum of –243 MPa within 180 thermal cycles. And then it gradually reduces to –30 MPa at the 300th thermal cycle.

11

σ_r displays a little relaxation because new microcracks and pores form as thermal cycle increases (see Fig. 5). The analysis shows that the evolution of σ_r near the coating surface with thermal cycles follows the relationship of $\sigma_r = -29.44 - 2.34N + 0.8 \times 10^{-2} N^2$. The current results before 180 thermal cycles are similar to that obtained by X-ray diffraction[35] and Raman spectroscopy methods [27], and theoretical results by Mao *et al.* [18], as shown in Fig. 11. Some difference may be ascribed to thermal treatment conditions, coating thickness and material components.

In the case of interface indentation (see Fig. 1(b)), K_{IC} in the coating close to the interface varies from the initial value of 0.19 to 0.81 MPa·m$^{1/2}$ before 100 thermal cycles, as shown in Fig. 10. Then K_{IC} gradually declines to 0.11 MPa·m$^{1/2}$ within the subsequent thermal cycles. Here we use a fitted parabola equation to describe the variation of K_{IC} with thermal cycling, i.e., $K_{IC} = 0.283 + 0.004N - 1.662 \times 10^{-5} N^2$. For as-received APS TBC systems, K_{IC} at the coating and bond coat interface was reported as 2.22 MPa·m$^{1/2}$ by a mixed-mode test [36], and 0.7 MPa·m$^{1/2}$ by a modified four-point bending test [37]. K_{IC} near the interface region is 1.1 MPa·m$^{1/2}$ after thermal treatment of 20 h [38]. Our experimental results by Vickers indentations are agreement with those available results. Moreover, it is clear that K_{IC} on the top coating surface are slightly larger than that around the coating/bond coat interface, which agrees well with the fact that the initial fracture in TBCs usually happens at interface [39]. Fig. 11 shows that the evolution of σ_r varies from the original value of –5 MPa to a maximum of –30 MPa within 204 thermal cycles. Then it gradually decreases to –9.6 MPa at the 300th thermal cycle due to the formation of micro-cracks. An empirical parabola equation fitted by experimental data can be obtained as $\sigma_r = -8.12 - 0.264N + 0.91 \times 10^{-3} N^2$. Our results agree with –75 MPa in YSZ, which was measured near the bond coating interface at 112 h by high-energy X-rays [40]. It is seen that all residual stresses in coating after thermal cycles are compressive, which accelerate the propagation of interface delamination or cracks, coating buckling and spallation of TBCs [41].

When indenter only acts on the lateral region of coating (see Fig. 1(c)), the evolution of K_{IC} and σ_r exhibits strong gradient characteristics. The effects of different locations L and thermal cycles N on K_{IC} are shown in Fig. 12. The values of K_{IC} close to the coating surface in an as-received sample ($N = 0$) are smaller than that near the interface. With the increase of thermal cycles, they firstly increase with different extents, and then gradually reduce to 0.3 MPa·m$^{1/2}$ at $N = 300$. It is worth noting that, from Figs. (10) and (12), the values of K_{IC} on lateral and interface regions in an APS TBC system are much smaller than that on the upper surface of coating under the same thermal cycling. The results may explain why the coating is so easy to delaminate and spall near the interface region in service. The improved Vickers indentation method as ''fingerprints'' can be applied to evaluate the "weakest" location of the coating, compared with other methods that usually analyze the mechanical properties of the coating as a whole. It is seen that K_{IC} in the coating presents strong anisotropic features due to the specially laminated structure by the APS technique and the sintering effect in high temperatures. Similarly, the influences of L and N on σ_r are shown in Fig. 13. The distributions of σ_r vary with different amplitudes along the thickness direction during thermal cycles. Under the same heat treatment condition, σ_r increases with the increase of L, which consists qualitatively with the results by neutron diffraction [42] and high-energy X-rays [40] methods.

5. Conclusions

In this paper, several major mechanical properties of an APS TBC system, including micro-hardness, fracture toughness and residual stress during thermal cycles, have been measured by a modified Vickers indentation device. The main conclusions can be summarized as follows:

(1) High-temperature sintering has an important influence on the evolution of Young's modulus, micro-hardness, fracture toughness and residual stress in TBCs. Young's modulus in coating varies from 50 to 120 GPa with increasing thermal cycling and then gradually decreases to 59 GPa, and

Young's modulus in the bond coat changes from 79 to 149 GPa. The values of Vickers hardness in coating increase from 2.76 to 6.14 GPa and decline to 4.4 GPa with increasing thermal cycling. In the bond coat, it increases from 3 to 4 GPa.

(2) Residual stresses play an important role in the determination of fracture toughness by the indentation method. On the top coating surface, fracture toughness changes in a range of 0.64 to 3.67 MPa·m$^{1/2}$. The corresponding residual stress varies from –36.8 to –243 MPa. In the lateral region of the top coating, fracture toughness changes in a range of 0.11 to 0.81 MPa·m$^{1/2}$. The corresponding residual stress varies from –5 to –30 MPa.

(3) The distributions of fracture toughness and residual stress along the coating thickness display strong gradient and anisotropic characteristics due to the typical laminated structure, which have been revealed by the modified Vickers apparatus.

References

[1] N. P. Padture, M. Gell, E. H. Jordan, Science, 296 (2002) 280-284.

[2] T. Liang, H. Guo, H. Peng, S. Gong, Surf Coat Technol, 205 (2011) 4374-4379.

[3] A. G. Evans, D. R. Mumm, J. W. Hutchinson, Prog Mater Sci, 46 (2001) 505-553.

[4] W. G. Mao, J. P. Jiang, Y. C. Zhou, C. Lu, Surf. Coat. Technol., 205 (2011) 3093-3102.

[5] J. T. DeMasi-Marcin, D. K. Gupta, Surf Coat Technol, 68-69 (1994) 1-9.

[6] G. R. Anstis, P. Chantikul, B. R. Lawn, D. B. Marshall, J Am Ceram Soc, 46 (1981) 533-538.

[7] D. B. Marshall, B. R. Lawn, J Am Ceram Soc, 60 (1976) 86-87.

[8] T. Y. Zhang, L. Q. Chen, R. Fu, Acta. Mater., 47 (1999) 3869-3878.

[9] J. Lesage, D. Chicot, Thin Solid Films, 415 (2002) 143-150.

[10] P. Chantikul, G. R. Anstis, B. R. Lawn, D. B. Marshall, J Am Ceram Soc, 64 (1981) 539-543.

[11] N. Lopez-Perrusquia, I. Campos-Silva, J. Martinez-Trinidad, A. Aviles, E. Alvarez-Castaneda, S. Juarez-Torres, Adv. Mater. Res., 65 (2009) 47-52.

[12] J. F. Li, X. Y. Wang, H. Liao, C. X. Ding, C. Coddet, J. Mater. Sci., 39 (2004) 7111-7114.

[13] M. Zhao, X. Chen, J. Yan, A. M. Karlsson, Acta Mater., 54 (2006) 2823-2832.

[14] P. Hivart, J. Crampon, Mech. Mater., 39 (2007) 998-1005.

[15] B. Lawn, R. Wilshaw, J. Mater. Sci., 10 (1975) 1049-1081.

[16] B. R. Lawn, E. R. Fuller, J Mater Sci, 19 (1984) 4061-4067.

[17] D. B. Marshall, B. R. Lawn, J Mater Sci, 14 (1979) 2001-2012.

[18] W. G. Mao, Y. C. Zhou, L. Yang, X. H. Yu, Mech. Mater., 38 (2006) 1118-1127.

[19] D. Chicot, P. Demarecaux, J. Lesage, Thin Solid Films, 283 (1996) 151-157.

[20] B. R. Lawn, A. G. Evans, D. B. Marshall, J. Am. Ceram. Soc., 63 (1980) 574-581.

[21] S. S. Kim, Y. H. Chae, S. Y. Choi, Tribol Lett, 17 (2004) 663-668.

[22] J. Lesage, D. Chicot, Thin Solid Films., 415 (2002) 143-150.

[23] D. Zhu, R. A. Miller, Surf Coat Technol, 108-109 (1998) 114-120.

[24] J. Gong, Ceram Int, 28 (2002) 767-772.

[25] S. Guo, Y. Kagawa, Scripta Mater., 50 (2004) 1401-1406.

[26] K. J. Yoon, S. J. Cho, J Mater Sci Lett, 12 (1993) 926-927.

[27] Q. Chen, W. G. Mao, Y. C. Zhou, C. Lu, Appl. Surf. Sci., 256 (2010) 7311-7315.

[28] W. G. Mao, Y. G. Shen, C. Lu, Scripta Mater., 65 (2011) 127-130.

[29] D. Zhu, R. Miller, J Therm Spray Technol, 9 (2000) 175-180.

[30] J. I. Eldridge, D. Zhu, R. A. Miller, J Am Ceram Soc, 84 (2001) 2737-2739.

[31] J. Haynes, M. Ferber, W. Porter, J Therm Spray Technol, 9 (2000) 38-48.

[32] S. Guo, Y. Kagawa, Ceram Int, 32 (2006) 263-270.

[33] S. R. Choi, D. Zhu, R. A. Miller, Eng. Fract. Mech., 72 (2005) 2144-2158.

[34] S. R. Choi, D. Zhu, R. A. Miller, NASA/TM-2004-212625, National Aeronautics and Space Administration, Glenn Research Center, Cleveland, OH, 2004.

[35] D. W. Jordan, K. T. Faber, Thin Solid Films, 235 (1993) 137-141.

[36] H. Deng, H. Shi, H. Yu, B. Zhong, SCIENCE CHINA Physics, Mechanics & Astronomy, 54 (2011) 618-624.

[37] P. F. Zhao, C. A. Sun, X. Y. Zhu, F. L. Shang, C. J. Li, Surf Coat Technol, 204 (2010) 4066-4074.

[38] A. Vasinonta, J. L. Beuth, Eng. Fract. Mech., 68 (2001) 843-860.

[39] J. Yan, A. M. Karlsson, M. Bartsch, X. Chen, Comp Mater Sci, 44 (2009) 1178-1191.

[40] C. M. Weyant, J. Almer, K. T. Faber, Acta Mater., 58 (2010) 943-951.

[41] W. G. Mao, C. Y. Dai, Y. C. Zhou, Q. X. Liu, Surf. Coat. Technol., 201 (2007) 6217-6227.

[42] J. Matejicek, S. Sampath, P. C. Brand, H. J. Prask, Acta Mater., 47 (1999) 607-617.

Fig. 1. (Color online) Schematics of three kinds of Vickers indentations on the top surface (a), near the interface region (b), and on the lateral region (c).

Fig. 2. (Color online) Evolution of Young's modulus in coating and bond coat with thermal cycles in nanoindentation tests.

Fig. 3. (Color online) Variation of Vickers hardness in coating and bond coat with thermal cycles.

Fig. 4. (Color online) Relationships of $P_i / c_i^{3/2}$ versus $c_i^{-1/2}$ under different thermal cycles when indented on the top coating surface.

Fig. 5. (Color online) The SEM observations of residual Vickers impression on the top coating surface under (a) $P = 296$ N and $N = 250$ h, and (b) $P = 296$ N and $N = 300$ h.

Fig. 6. (Color online) Influence of thermal cycles on the fitting of $P_i / c_i^{3/2}$ versus $c_i^{1/2}$ when indented near the coating/bond coat interface.

Fig. 7. (Color online) The SEM image of residual Vickers impression morphology near the interface region with $P = 98$ N and $N = 150$ h.

Fig. 8. (Color online) Plots of $P_i / c_i^{3/2}$ versus $c_i^{1/2}$ with the increase of thermal cycles on the lateral region of coating.

Fig. 9. (Color online) The SEM image of residual Vickers impression morphology near the lateral region with $P = 98$ N and $N = 204$ h.

Fig. 10. (Color online) Variation of fracture toughness in coating with thermal cycles.

Fig. 11. (Color online) Distribution of the corresponding residual stress in coating as a function of thermal cycles.

Fig. 12. (Color online) The gradient distribution of fracture toughness along the thickness direction under different thermal cycles.

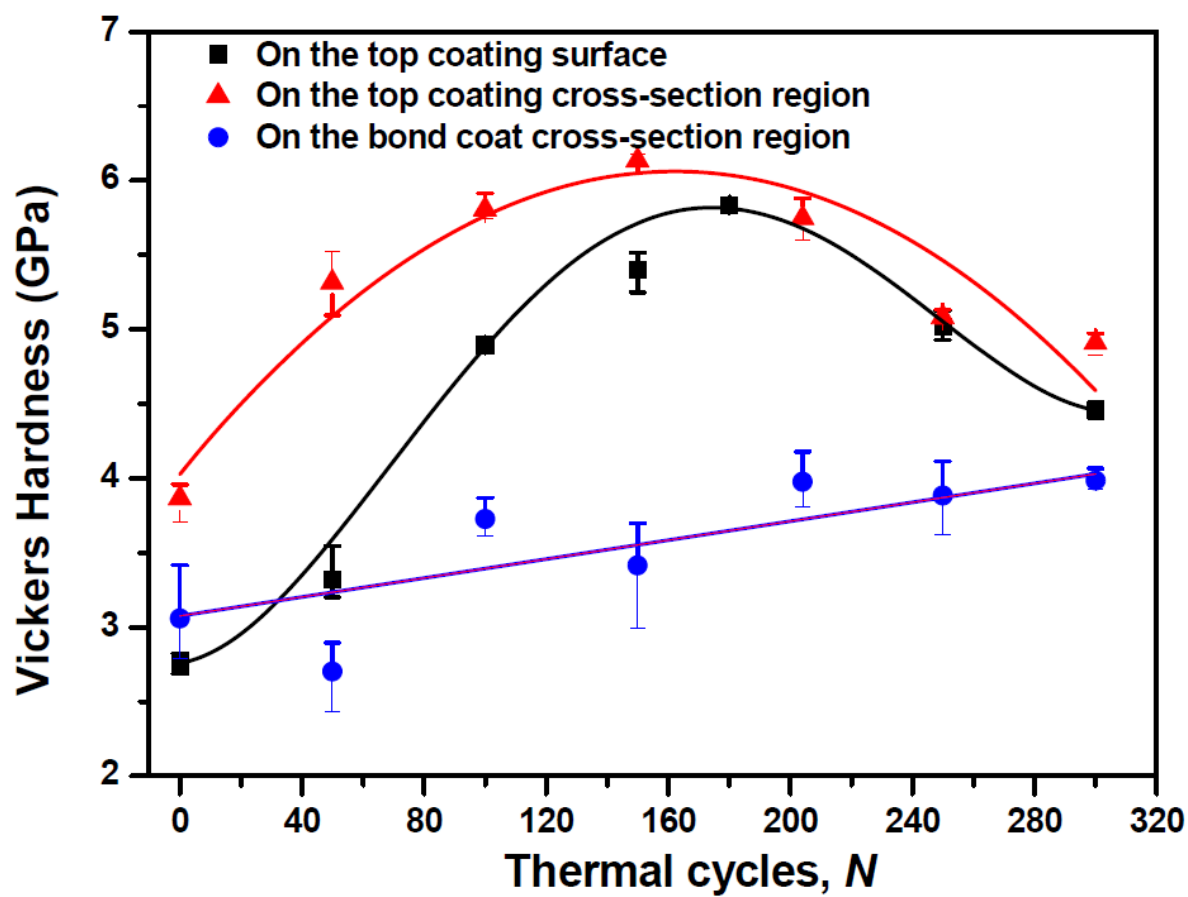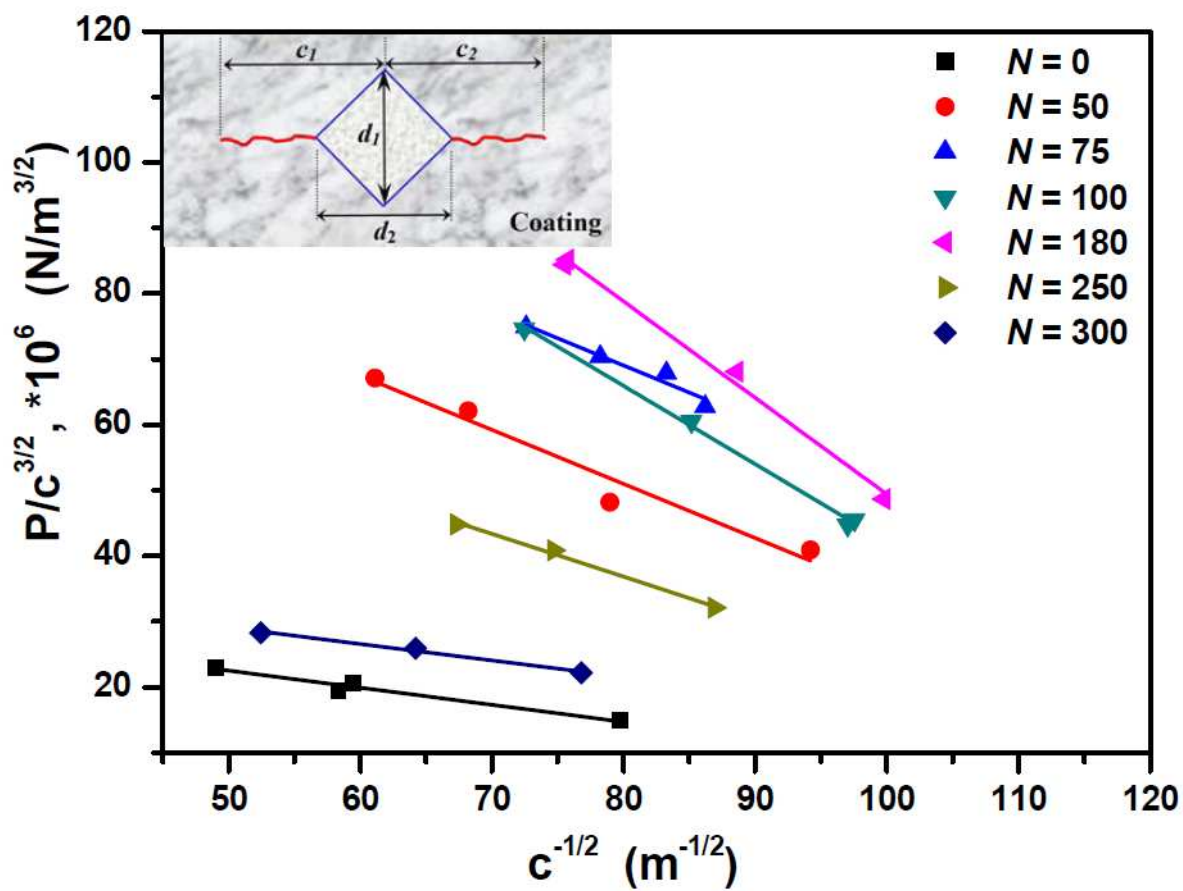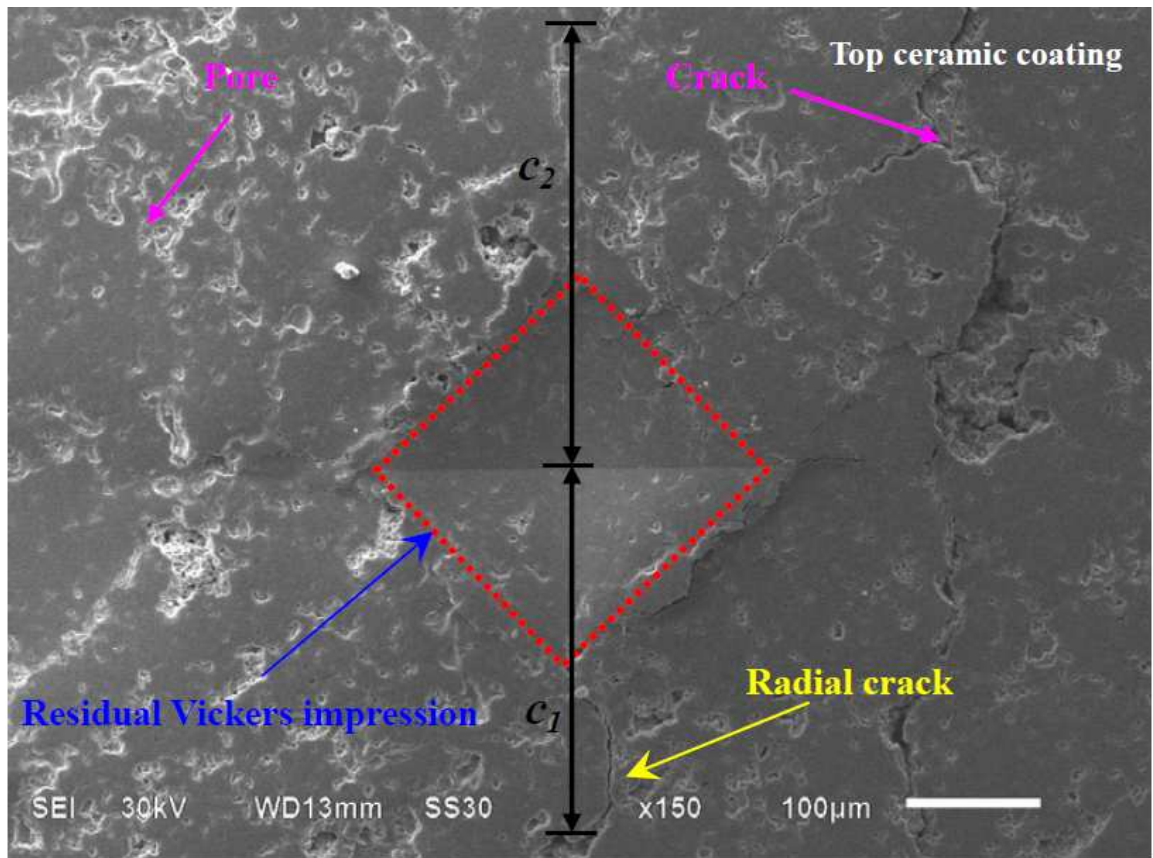Fig. 13. (Color online) The gradient distribution of the corresponding residual stress on the coating cross-section with thermal cycles.
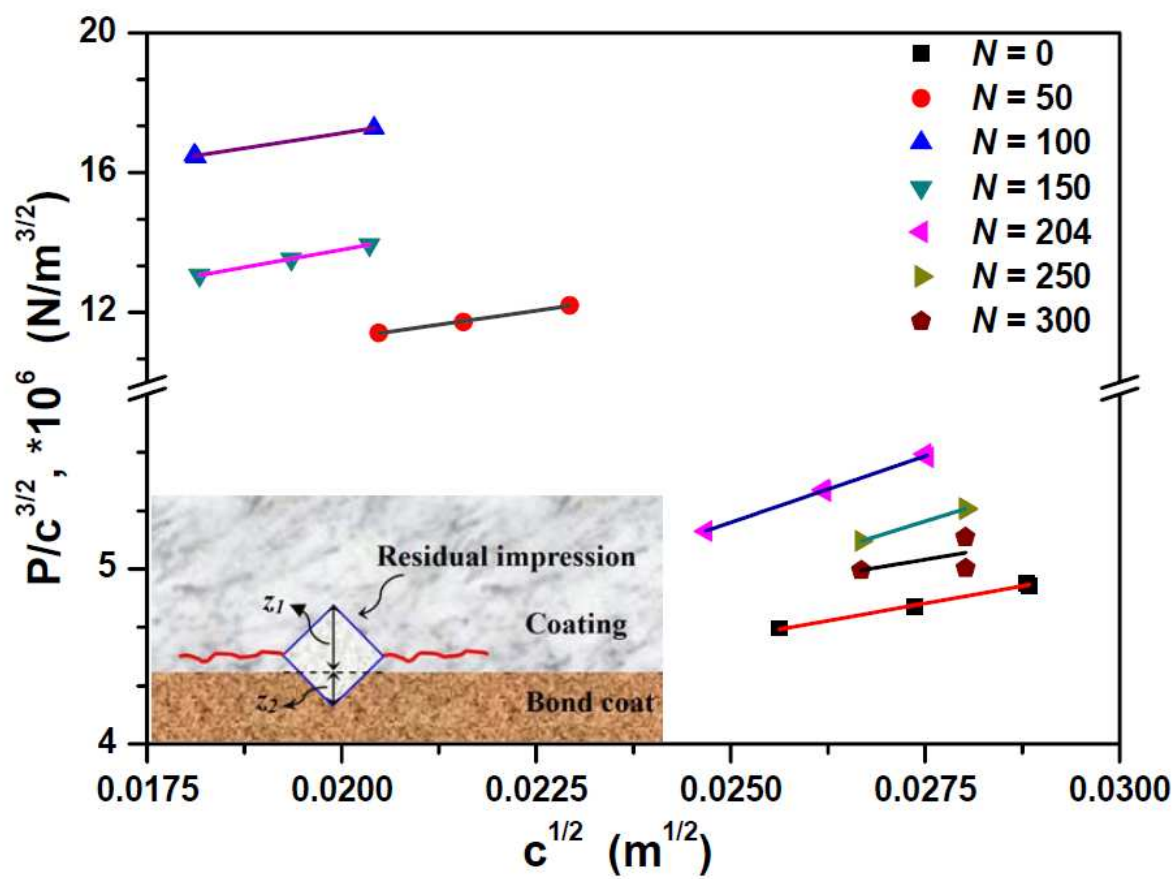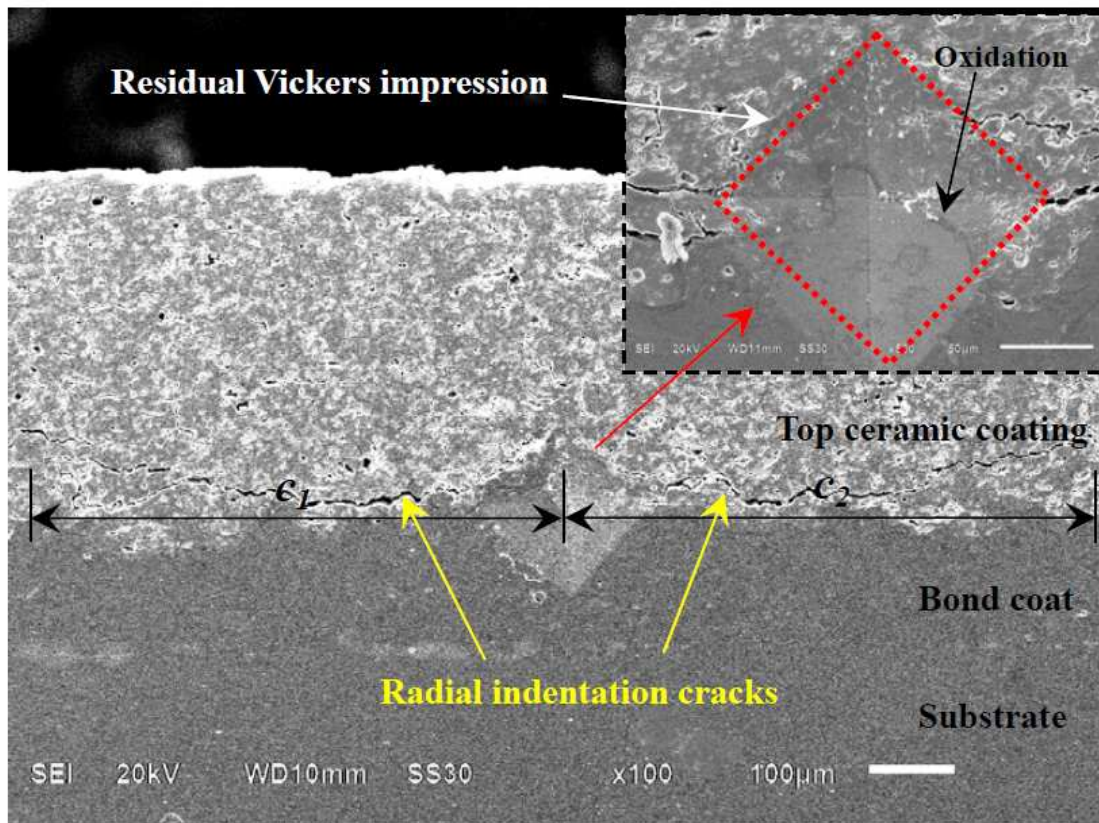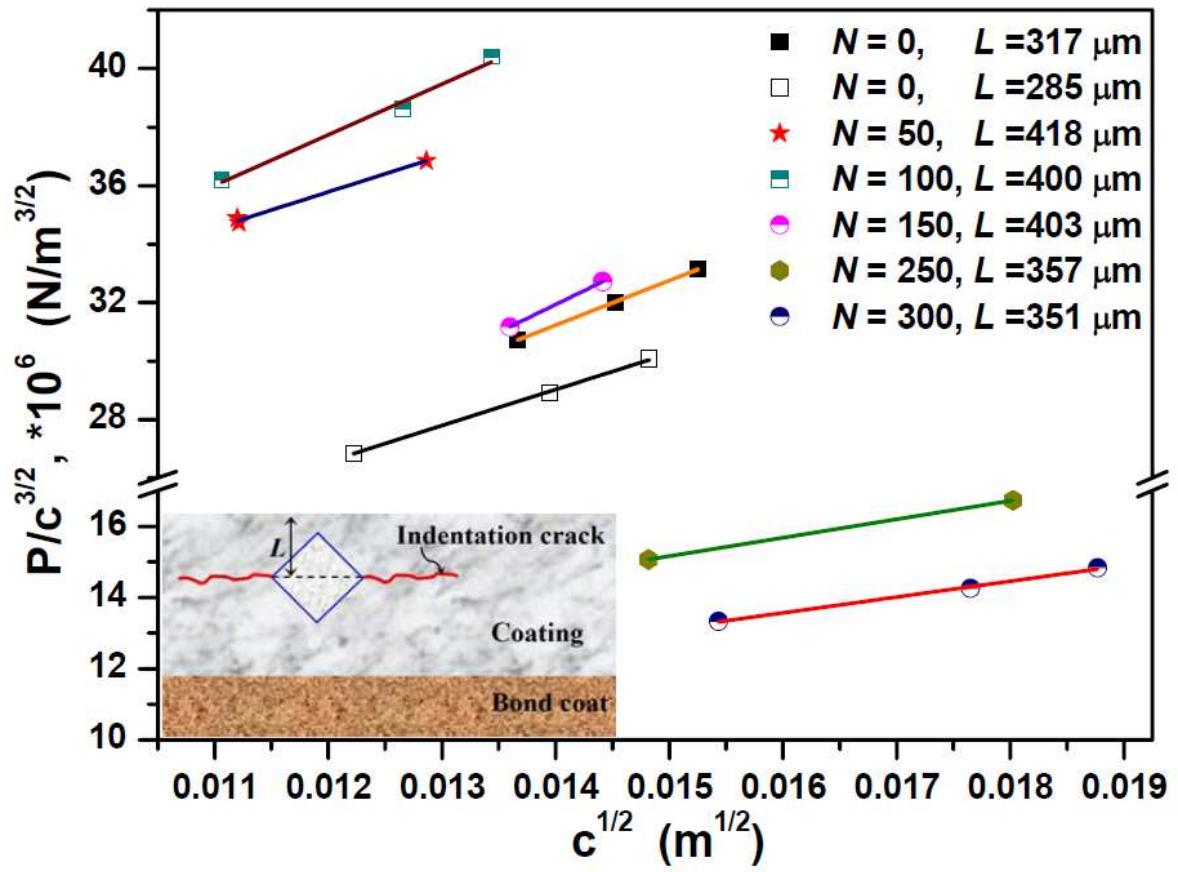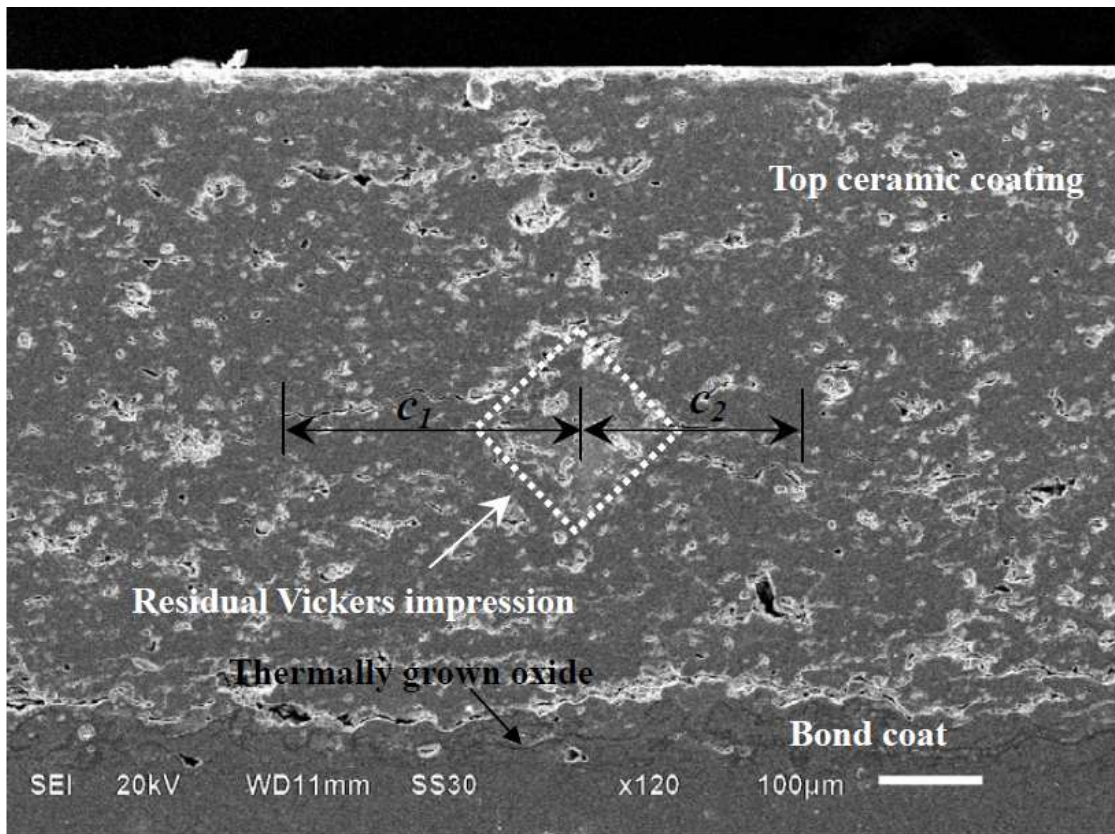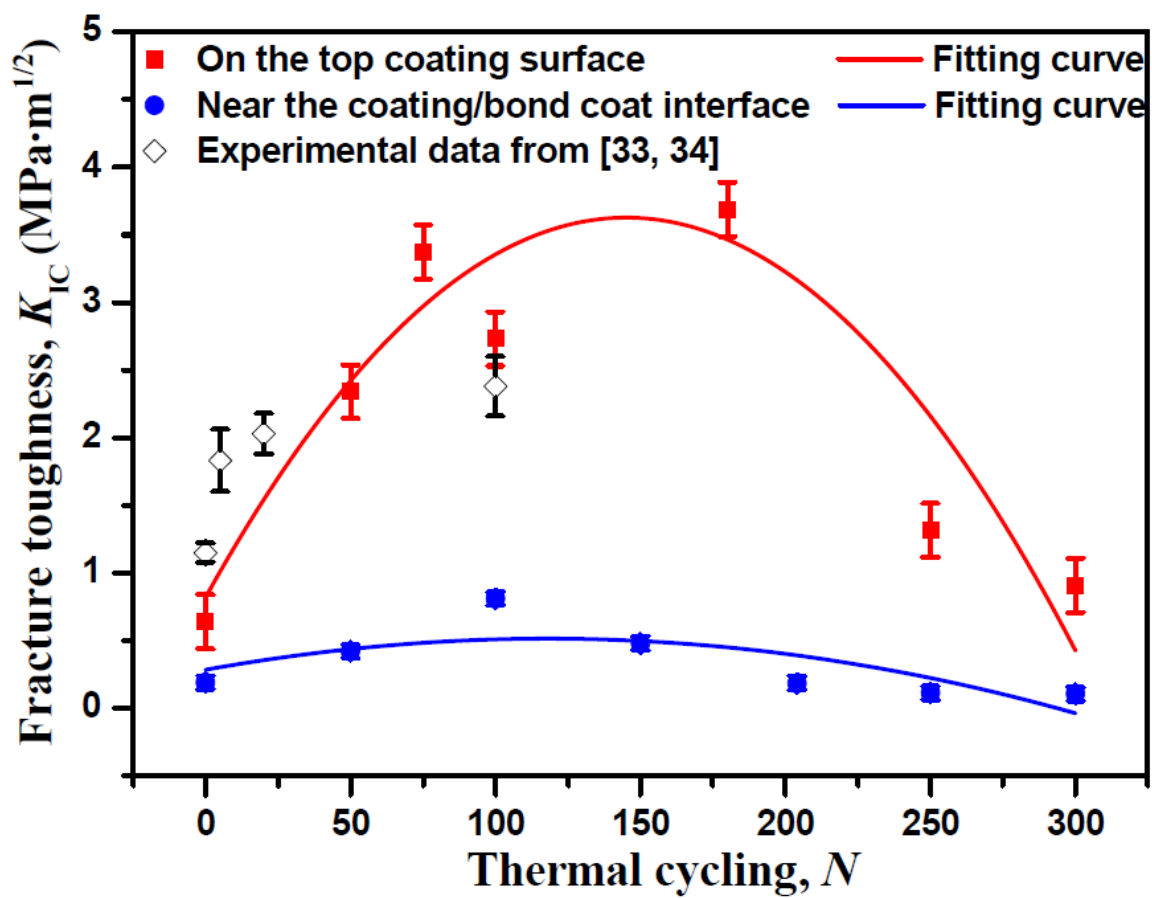
Fig. 1

Fig. 2

19
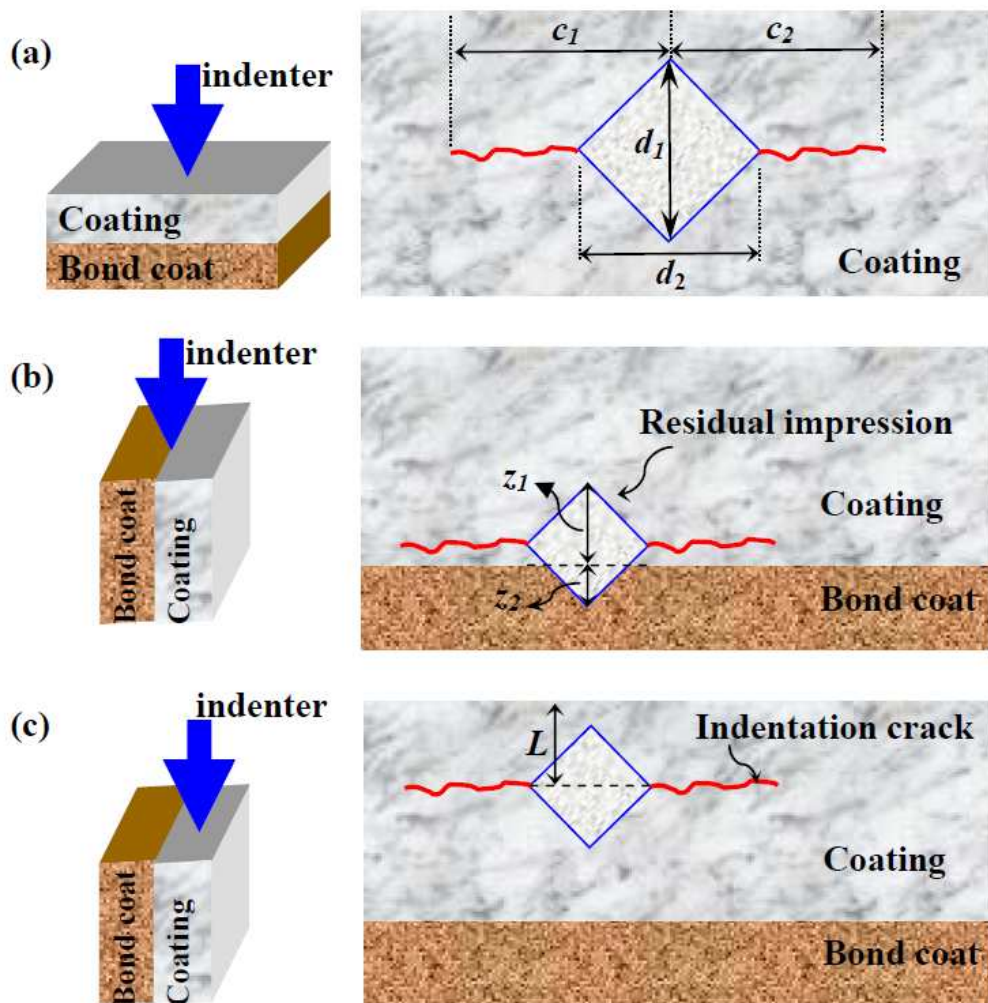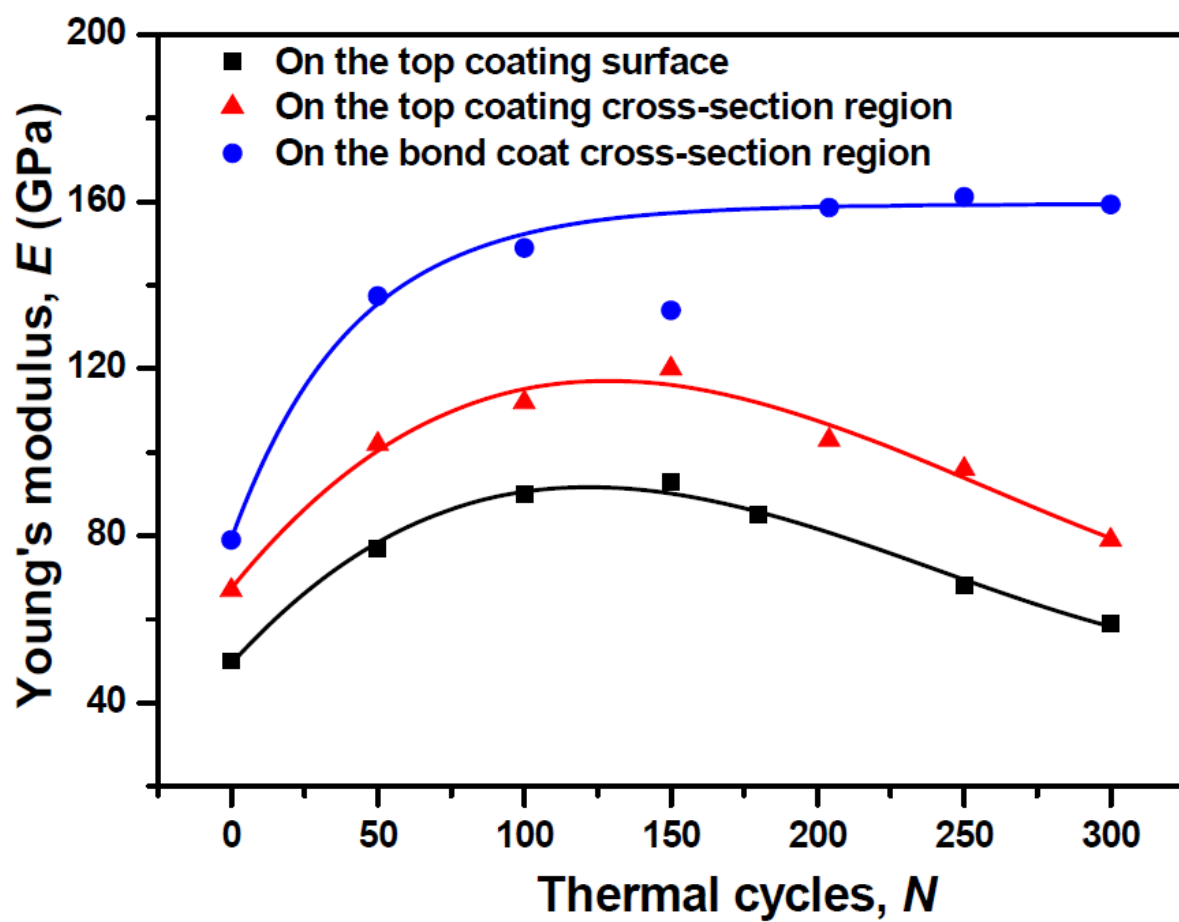
Fig. 3

Fig. 4

Fig. 5

Fig. 6

Fig. 7

Fig. 8

Fig. 9

Fig. 10

Fig. 11

Fig. 12

29

Fig. 13